Supplementary file

Carbon quantum dots-titanium doped strontium ferrite nanocomposite: Visible light active photocatalyst to degrade nitroaromatics

Jaspreet Kaur Grewal[1,a], Manpreet Kaur[1,*], Kousik Mandal[2,b], and Virender K. Sharma [3,**]

[1]Department of Chemistry, Punjab Agricultural University, Ludhiana, 141001, Punjab, India

[2]Department of Entomology, Punjab Agricultural University, Ludhiana, 141001, Punjab, India

[3]Program for Environment and Sustainability, Department of Environmental and Occupational Health, School of Public Health, Texas A&M University (TAMU), College Station, TX 77843-1266, USA

[a] jaspreet-1762002@pau.edu

[b]kousik30@pau.edu

Correspondence: *manpreetchem@pau.edu, **vsharma@tamu.edu

Text S1

Comparative evaluation of undoped and titanium doped strontium ferrite NPs

$Sr_{0.4}Ti_{0.6}Fe_2O_{4.6}$ NPs with higher Ti^{4+} content. displayed a higher photocatalytic efficiency as compared to pristine $SrFe_2O_4$, $TiFe_2O_5$ and $Sr_{0.7}Ti_{0.3}Fe_2O_{4.3}$ NPs. The photocatalytic degradation efficiency of pristine $SrFe_2O_4$ NPs for studied nitroaromatic compounds ranged between 52.0 % to 68.0% and it increased significantly to 69.2% - 89.4% for $Sr_{0.4}Ti_{0.6}Fe_2O_{4.6}$ NPs. The higher photocatalytic efficiency of $Sr_{0.4}Ti_{0.6}Fe_2O_{4.6}$ NPs (Figure S1d-f) could also be ascribed to the generation of cationic vacancies and oxygen hyperstoichiometry that enhances the photocatalytic potential by providing a heterogeneous surface to the nanomaterial. The Ti^{4+} substituents acted as electron acceptors due to more positive charge on them, thus preventing the recombination of photo-generated e^- and h^+ pairs and consequently led to the improvement of photocatalytic degradation. These studies displayed the $Sr_{0.4}Ti_{0.6}Fe_2O_{4.6}$ NPs as the best photocatalyst and hence used for conducting the further studies.

Text S2

Influence of catalyst dose

In case of *p*-nitrophenol, pendimethalin and martius yellow, the catalyst dose of CQDs-$Sr_{0.4}Ti_{0.6}Fe_2O_{4.6}$ nanocomposite was varied from 0.02 g/L to 1.0 g/L at the optimized pH of 3.0. It was observed that the rate of photodegradation increased proportionally with the amount of catalyst added upto 0.2 g/L due to the increased number of active photocatalytic sites. However, as the catalyst loading increase beyond 0.2 g/L, the photocatalytic rate decreased due to an increased tendency toward aggregation, *i.e.* particle-particle interaction increased while the surface area available for light absorption decreased. Furthermore, the high frequency of CQDs-$Sr_{0.4}Ti_{0.6}Fe_2O_{4.6}$ photocatalyst crumbs floating in nitroaromatic pollutants solutions inhibited the visible light penetration. As a result, no additional light could access the surface

of the photocatalyst since the surrounding grains would provide shade (Wu and Zhang 2019). Hence, the lesser penetration of light led to reduced exposure area and consequently resulted into reduced photoactivity. The comparative photocatalytic degradation of nitroaromatic pollutants using is presented in Figure 6f. It was observed that CQDs-$Sr_{0.4}Ti_{0.6}Fe_2O_{4.6}$ nanocomposite displayed the maximum (%) photodegradation efficiency of 90.4 %, 94.5 % and 96.8 % at 0.2 g/L of catalyst dose for martius yellow, *p*-nitrophenol and pendimethalin, respectively.

Text S3

Characterization tools

The magnetic properties of the materials (x = 0.0, 0.3, 0.6 & 1.0) were determined by vibrating sample magnetometer (VSM Model, PAR-155). The XRD, Panlytical X'pert Pro with Cu Kα radiations (λ = 1.5404 A^o) was used to determine the phase constitutes of the fabricated catalysts. The micromorphology of the obtained powders was detected by TEM model Hitachi Hi-7650 and SEM model Hitachi S-3400 whereas the EDX images were recorded on thermo Noran System utilizing point and shoot method. Quantachrome Nova-1000 was used to carry out the nitrogen adsorption-desorption experiments and BET (Brunauer-Emmett-Teller) specific surface area of the fabricated ferrites was determined based on the obtained isotherm data. Dynamic light scattering and zeta potential analysis were recorded by using Zetasizer Nano- ZS to determine particle size distribution and stability of colloidal dispersions. FT-IR measurements were carried out on on Perkin Elmer, Model RX-1 FT-IR Spectrophotometer using KBr pellets, in the wave number ranging between 4000-400 cm^{-1}. Fluorescence spectra were recorded using Agilent Cary Eclipse Fluorescence spectrophotometer. The residual concentration of *p*-nitrophenol, pendimethalin and martius yellow solutions were determined by UV-visible spectrophotometer (UV-1800 Shimadzu UV-

visible) at wavelengths of 398, 465 and 445 nm, respectively. The Mössbauer spectra were recorded with least square fitting using commercially available program ' MOSSWIN'.

Text S4

Synthesis of $Sr_{0.4}Ti_{0.6}Fe_2O_{4.6}$ nanoparticles (NPs)

The $Sr_{0.4}Ti_{0.6}Fe_2O_{4.6}$ NPs were synthesized using sol-gel method by dissolving the required stoichiometric molar ratios of $Fe(NO_3)_3.9H_2O$ (8.08g), $Sr(NO_3)_2 \cdot 6H_2O$ (1.48 g) and $CH_3(CH_2)_3O)_4Ti$ (1.02 ml) in 20 ml of deionized water. 1.31 mol of citric acid was added in aqueous solution. To achieve the desired pH of 7.0, NH_4OH solution was added to the aforementioned solution and magnetically stirred at 60 °C until the solution turned into sol. The sol transformed into gel after 8.0 hrs of stirring; the gel was then dried for 12 hrs at 100°C,. The dried gel was then crushed and subjected to a 3.0 hour calcination process at 300 °C to produce the final product, $Sr_{0.4}Ti_{0.6}Fe_2O_{4.6}$.

Text S5

Adsorption experiments

The preliminary adsorption experiments were conducted for comparing the efficacy of CQDs, $Sr_{0.4}Ti_{0.6}Fe_2O_{4.6}$, NPs and their nanocomposite CQDs-$Sr_{0.4}Ti_{0.6}Fe_2O_{4.6}$ (with 2:1 w/w ratio). The solution pH was modulated using 0.1 N NaOH and 0.1 N HCl. The residual contents of *p*-nitrophenol, pendimethalin and martius yellow were analyzed using UV–Visible spectrophotometer at 398, 465 and 445 nm, respectively. All the experiments were performed in triplicates and their average values are reported. The removal efficiencies were evaluated using equations (1);

$$\text{Removal (\%)} = C_o - C_e / C_o \times 100 \ldots\ldots. (1)$$

where C_o and C_e are initial and equilibrium contaminant concentrations in mg/L, respectively.

Figure S3 demonstrates the effect of pH for evaluating the efficiencies of synthesized nanomaterials for the adsorption of *p*-nitrophenol, pendimethalin and martius yellow. The surface potential at pH 3.0 was found to be more positive for CQDs-$Sr_{0.4}Ti_{0.6}Fe_2O_{4.6}$ nanocomposite (+ 35.40 mV) as compared to CQDs and $Sr_{0.4}Ti_{0.6}Fe_2O_{4.6}$ NPs (Figure 5c). The nanocomposite showed the highest adsorption efficiency (92.1% for *p*-nitrophenol; 99.2% for pendimethalin; 88.4% for martius yellow). The higher adsorption potential of CQDs-$Sr_{0.4}Ti_{0.6}Fe_2O_{4.6}$ nanocomposite was due to electrostatic attractions among the anionic nitroaromatic pollutants and the positive surfaces of the nanocomposite. A similar trend was observed in studying the adsorption of anionic dye using $MgFe_2O_4$-bentonite nanocomposite (Khusboo et al. [1]). However, to avoid extremely acidic conditions, pH 3.0 was optimized for further experiments.

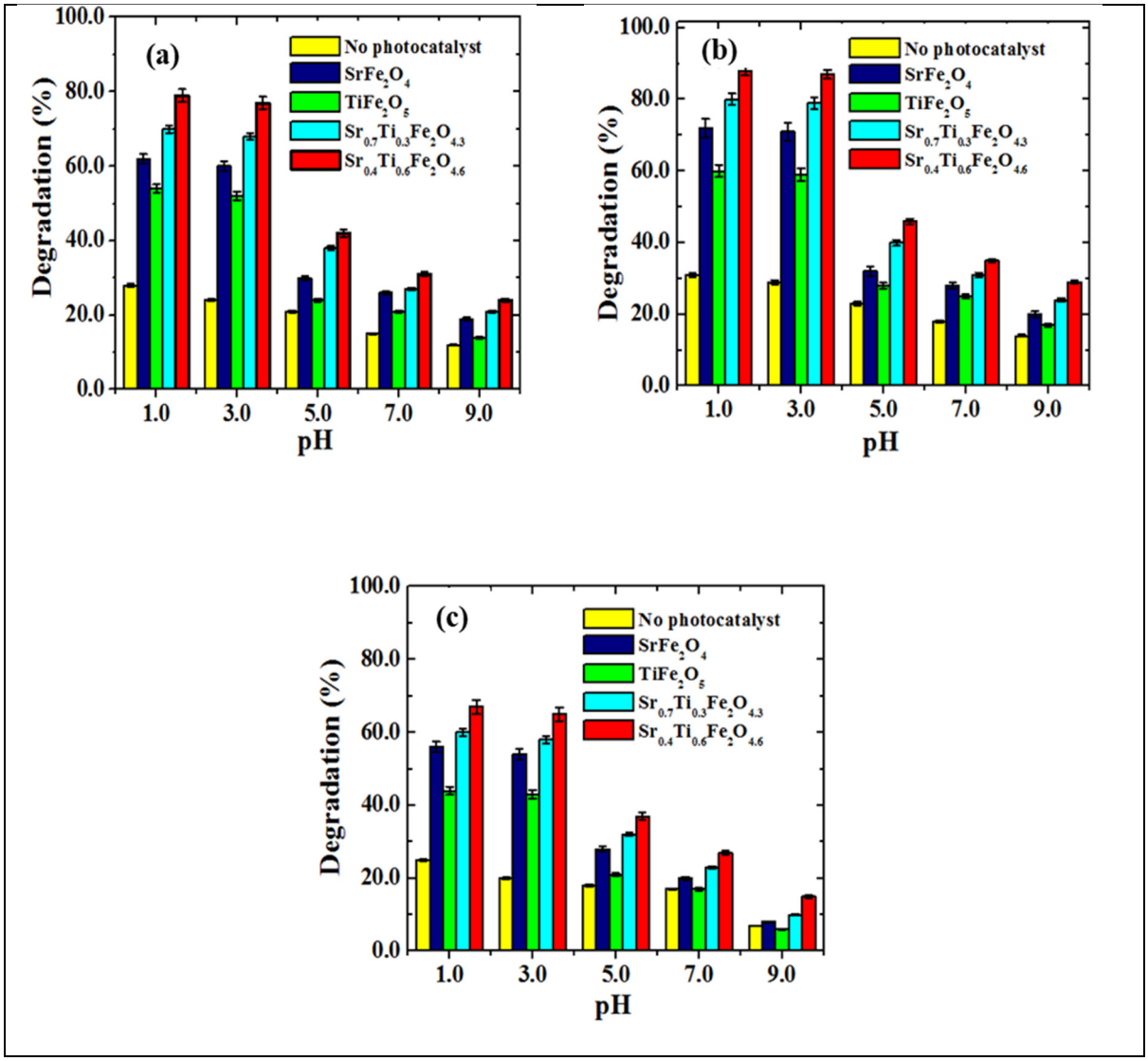

Figure S1 Photocatalytic degradation of (a) *p*-nitrophenol, (b) pendimethalin and (c) martius yellow under visible light irradiation using $SrFe_2O_4$, $TiFe_2O_5$, $Sr_{0.7}Ti_{0.3}Fe_2O_{4.3}$ and $Sr_{0.4}Ti_{0.6}Fe_2O_{4.6}$ NPs (Experimental conditions: catalyst dose, 0.2 g/L; irradiation time, 2 hours and concentration 2.0 mg/L (*p*-nitrophenol and pendimethalin) and 0.2 mg/L (martius yellow)

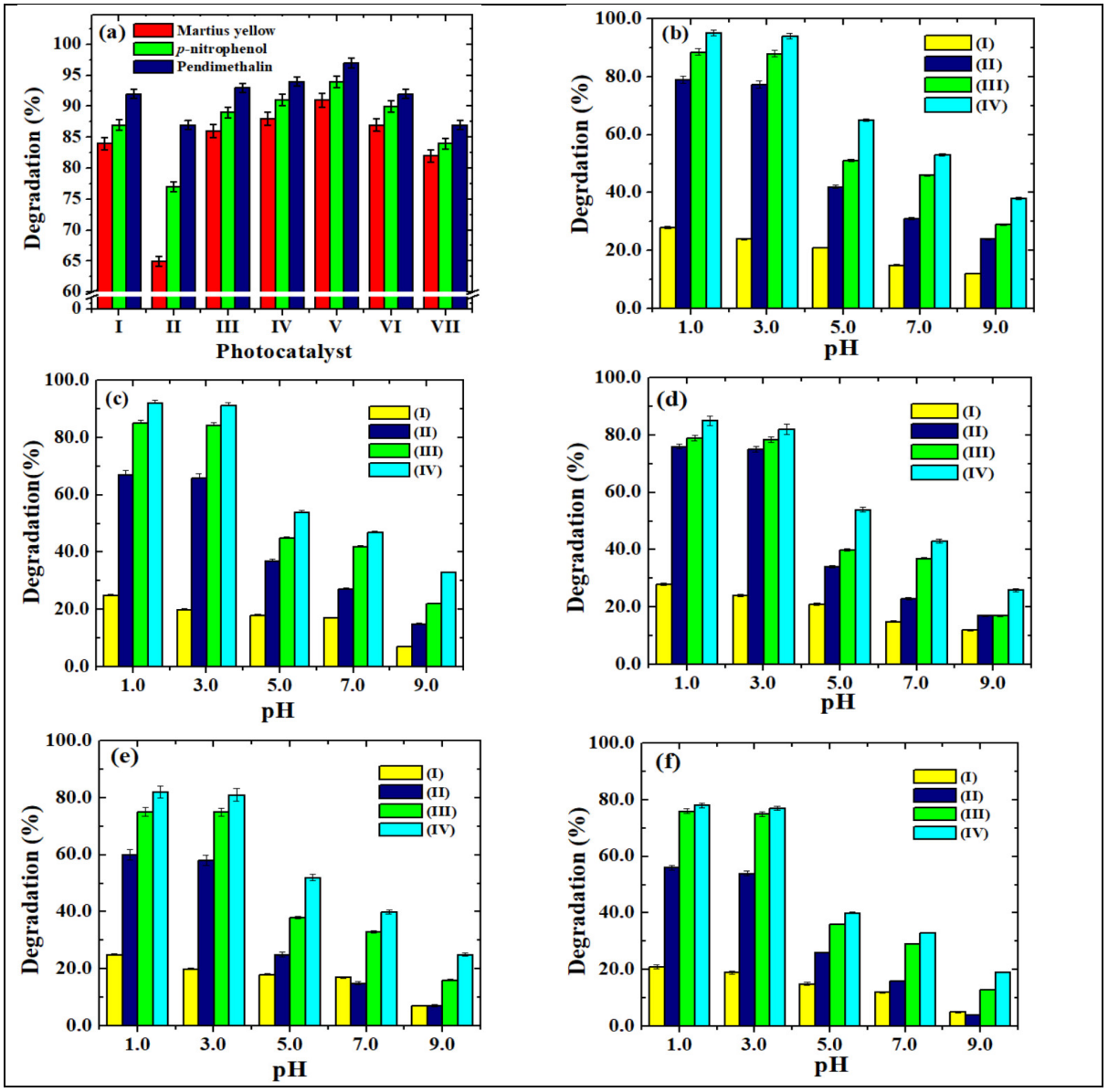

Figure S2 (a) Photocatalytic degradation of *p*-nitrophenol, pendimethalin and martius yellow using (I) CQDs, (II) $Sr_{0.4}Ti_{0.6}Fe_2O_{4.6}$, (III) CQDs-$Sr_{0.4}Ti_{0.6}Fe_2O_{4.6}$ nanocomposite (0.5: 1.0 w/w ratio), (IV) CQDs-$Sr_{0.4}Ti_{0.6}Fe_2O_{4.6}$ nanocomposite (1.0: 1.0 w/w ratio), (V) CQDs-$Sr_{0.4}Ti_{0.6}Fe_2O_{4.6}$ nanocomposite (1.0: 2.0 w/w ratio), (VI) CQDs-$Sr_{0.4}Ti_{0.6}Fe_2O_{4.6}$ nanocomposite (4.0: 1.0 w/w ratio), (VII) CQDs-$Sr_{0.4}Ti_{0.6}Fe_2O_{4.6}$ nanocomposite (8.0: 1.0 w/w ratio); Photocatalytic degradation of (b) *p*-nitrophenol, (c) martius yellow under visible light irradiation, (d) pendimethalin, (e) *p*-nitrophenol and (f) martius yellow under ultraviolet irradiation (I) without photocatalyst, (II) $Sr_{0.4}Ti_{0.6}Fe_2O_{4.6}$, (III) CQDs, (IV) CQDs-$Sr_{0.4}Ti_{0.6}Fe_2O_{4.6}$ nanocomposite (2.0: 1.0 w/w ratio) (Experimental conditions: catalyst dose, 0.2 g/L; irradiation time, 2 hours and concentration 2.0 mg/L (*p*-nitrophenol and pendimethalin and 0.2 mg/L (martius yellow)

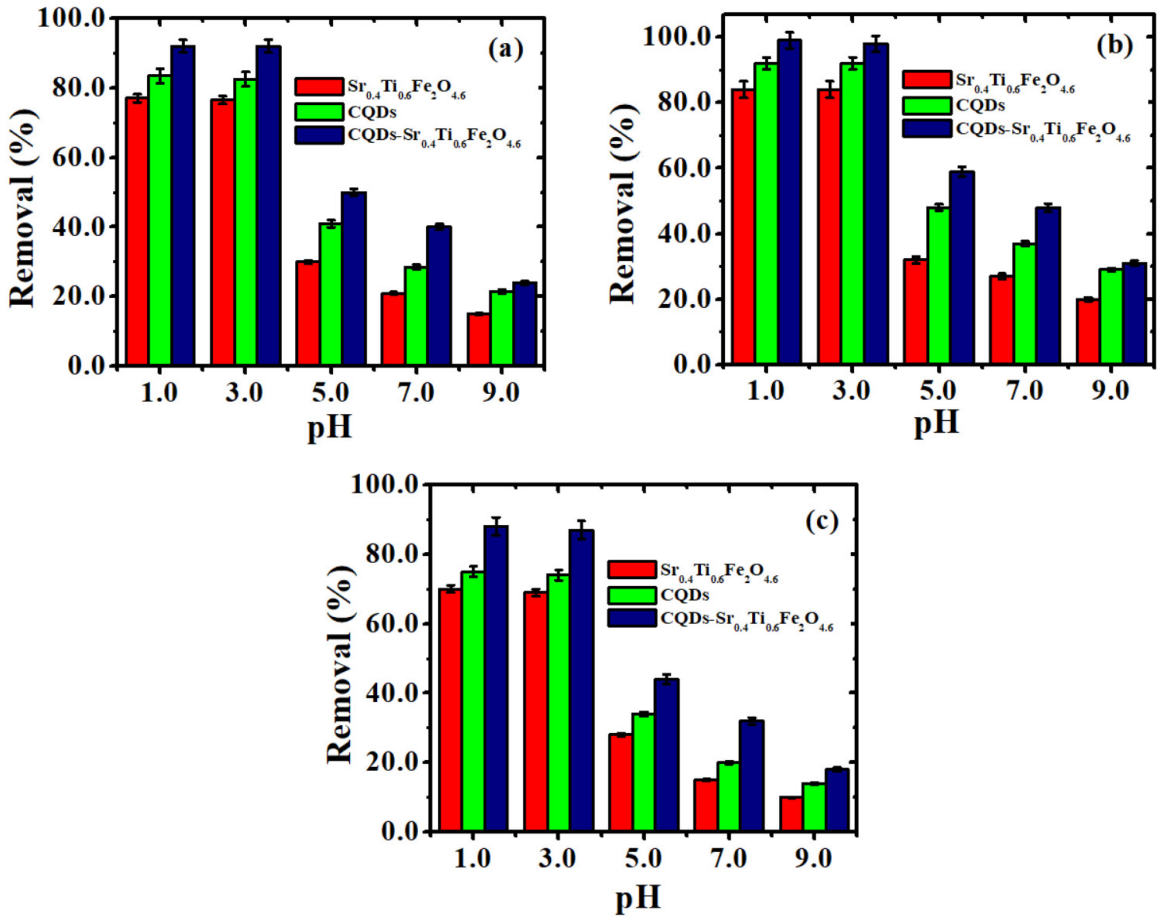

Figure S3 Removal efficiency of (a) *p*-nitrophenol, (b) pendimethalin and (c) martius yellow using CQDs, $Sr_{0.4}Ti_{0.6}Fe_2O_{4.6}$ and CQDs-$Sr_{0.4}Ti_{0.6}Fe_2O_{4.6}$ nanocomposite (2.0: 1.0 w/w ratio), (Experimental conditions: adsorbent dose, 0.1 g/L; contact time, 2 hours and concentration 2.0 mg/L (*p*-nitrophenol and pendimethalin and 0.2 mg/L (martius yellow)

Table S1: Comparison of the quantum yield values using different agricultural waste products

Precursor Material	Synthesis Method	Quantum Yield (%)	Ref.
Mango peel	Hydrothermal	8.5	[2]
Orange waste peels	Hydrothermal	11.37	[3]
Purslane leaves	Hydrothermal	12.5	[4]
Sugarcane bagasse	Hydrothermal	17.9	[5]
Onion waste	Hydrothermal	28.0	[6]
Waste biomass	Ultrasonication-assisted chemical oxidation method	4.45-26.2	[7]
Tamarindus indica leaves	Hydrothermal	46.6	[8]
Waste biomass	Hydrothermal	76.9	[9]
Sugarcane bagasse	Solvothermal	78.9	Present work

References

[1] Khusboo, Kaur, M.; Kiranjeet. Mechanistic insight into adsorption and photocatalytic potential of magnesium ferrite-bentonite nanocomposite, J. Photochem. Photobiol. A Chem. 2022, 425, 113717.

[2] Jiao, X.Y.; Li, L.S.; Qin, S.; Zhang, Y.; Huang, K.; Xu, L. The synthesis of fluorescent carbon dots from mango peel and their multiple applications. *Colloids Surf. A Physicochem. Eng. Asp*. **2019**, *577*, 306–314.

[3] Surendran, P.; Lakshmanan, A.; Vinitha, G.; Ramalingam, G.; Rameshkumar, P. Facile preparation of high fluorescent carbon quantum dots from orange waste peels for nonlinear optical applications. *Luminescence* **2019**, *35*, 196–202.

[4] Wael A. A.; Ahmed F. R.; Mona E. A.; Nagy L. T.; Ahmed S. A.; Mohamad M. A. Green synthesis of carbon quantum dots from purslane leaves for the detection of formaldehyde using quartz crystal microbalance. *Carbon* **2021***, 179,* 159-171.

[5] Pandiyan, S.; Arumugam, L.; Srirengan, S. P.; Pitchan, R.; Sevugan, P.; Kannan, K.; Pitchan, G.; Hegde, T. A.; Gandhirajan, V. Biocompatible Carbon Quantum Dots Derived from Sugarcane Industrial Wastes for Effective Nonlinear Optical Behavior and Antimicrobial Activity Applications. *ACS Omega,* **2020,** *5(47),* 30363-30372.

[6] Bandi, R.; Gangapuram, B.R.; Dadigala, R.; Eslavath, R.; Singh, S.S.; Guttena, V. Facile and green synthesis of fluorescent carbon dots from onion waste and their potential applications as sensor and multicolour imaging agents. *RSC Adv.* **2016**, *6*, 28633–28639.

[7] Boruah, A.; Saikia, M.; Das, T.; Goswamee, R. L.; Saikia, B. K. Blue-emitting fluorescent carbon quantum dots from waste biomass sources and their application in fluoride ion detection in water. *J. Photochem. Photobiol. B: Biol.* **2020***, 209,* 111940.

[8] Bano, D.; Kumar, V.; Singh, V. K.; Hasan, S. H. Green synthesis of fluorescent carbon quantum dots for the detection of mercury (II) and glutathione. *New J. Chem.* **2018***, 42,* 5814-5821.

[9] Jing, S.; Zhao, Y.; Sun, R. C.; Zhong, L.; Peng, X. Facile and High-yield Synthesis of Carbon Quantum Dots from Biomass-derived Carbons at Mild Condition. *ACS Sustain. Chem. Eng.* **2019,** *7(8)***,** 7833-7843**.**